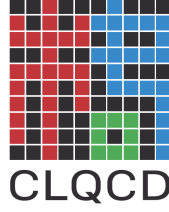


Accurate nucleon iso-vector scalar and tensor charge at physical point (CLQCD Collaboration)



Ji-Hao Wang,^{1,2} Zhi-Cheng Hu,^{3,2} Xiangdong Ji,⁴ Xiangyu Jiang,¹ Yushan Su,^{4,*} Peng Sun,³ and Yi-Bo Yang^{1,2,5,6,†}

¹*CAS Key Laboratory of Theoretical Physics, Institute of Theoretical Physics, Chinese Academy of Sciences, Beijing 100190, China*

²*University of Chinese Academy of Sciences, School of Physical Sciences, Beijing 100049, China*

³*Institute of Modern Physics, Chinese Academy of Sciences, Lanzhou, 730000, China*

⁴*Department of Physics, University of Maryland, College Park, MD 20850, USA.*

⁵*School of Fundamental Physics and Mathematical Sciences,*

Hangzhou Institute for Advanced Study, UCAS, Hangzhou 310024, China

⁶*International Centre for Theoretical Physics Asia-Pacific, Beijing/Hangzhou, China*

(Dated: November 5, 2025)

We report a new high precision calculation of the isospin vector charge $g_{S,T}$ of the nucleon using recently proposed “blending” method which provides a high-accuracy stochastic estimate of the all-to-all fermion propagator. By combining the current-involved interpolation operator, which can efficiently cancel the major excited state contamination, we can extract high-precision g_S and g_T directly at the physical pion mass. Using 15 of the $N_f = 2 + 1$ lattice ensembles which covers 5 lattice spacing, 5 combinations with the same quark masses and lattice spacing but multiple volumes, and includes three at the physical pion mass, we report so far most accurate lattice QCD prediction $g_T^{\text{QCD}} = 1.0258[79]_{\text{tot}}(56)_{\text{stat}}(24)_a(44)_{\text{FV}}(01)_\chi(24)_{\text{ex}}(05)_{\text{re}}$ and $g_S^{\text{QCD}} = 1.107[47]_{\text{tot}}(32)_{\text{stat}}(04)_a(29)_{\text{FV}}(01)_\chi(18)_{\text{ex}}(08)_{\text{re}}$ at $\overline{\text{MS}}$ 2 GeV, with the systematic uncertainty from continuum, infinite volume, chiral extrapolations, excited state contamination and also renormalization.

Introduction: A wide range of experiments use nucleons and nuclei as targets to probe the limits of the Standard Model and search for new physics. Interpreting the results from these experiments requires precise knowledge of the matrix elements that describe how a target interacts with a probe (like a current or an effective operator). Obtaining those matrix elements with percent-level uncertainty, is essential for the precision test of the standard model and can only be done by the first-principle lattice QCD calculation.

The nucleon iso-vector charges $\bar{u}\Gamma u - \bar{d}\Gamma d$ —specifically for the axial-vector ($\Gamma = \gamma_5\gamma_i$), scalar ($\Gamma = \mathcal{I}$), and tensor ($\Gamma = \sigma_{ij}$) currents—are among the simplest matrix elements to compute. This simplicity arises because the disconnected quark diagrams cancel out, up to isospin-breaking (ISB) effects. While the axial current can be tightly constrained from neutron weak decay, modulo ISB and QED corrections [1], the scalar and tensor charges are in higher demand. They are particularly crucial for probing TeV-scale new physics [2, 3], enabling high-precision calculations of the proton-neutron mass differ-

ence [4], and providing constraints on parton distribution functions [5, 6].

However, precise predictions of these charges remain highly challenging. This is primarily due to the competing difficulties of significant excited-state contamination (ESC) at small source-sink separations (t_f) and exponentially growing statistical noise at large t_f . Consequently, although sophisticated methods (e.g., multi-state fits (e.g., [7, 8]), multi-channel analyses through generalized eigen value problem (GEVP) with πN [9, 10] and/or σN states [11], Feynman-Hellman inspired method [12]) exist, the community has not yet converged on a definitive criterion for ensuring ESC is sufficiently suppressed in realistic calculations [13].

At the same time, a critical limitation of all existing high-precision lattice QCD results for $g_{A,S,T}$ [8, 12, 14–16] is their dependence on the χ PT ansatz for the chiral extrapolation and also finite-volume effects (FVE) [17]. This model imposes a specific suppression of FVE at physical quark masses, an assumption not sufficiently constrained by the lattice data around physical pion mass which has sizable statistical uncertainty. This dependence therefore represents a uncontrolled source of systematic error in the field.

Using the blending method [18] and the idea of current-

* Corresponding author: ysu12345@umd.edu

† Corresponding author: ybyang@itp.ac.cn

involved interpolation field [11, 19] proposed recently, our study delivers a new calculation of the nucleon iso-vector charges g_S and g_T with better control over systematic errors—notably from ESC, chiral extrapolation and FVE—compared to all existing lattice determinations. This advancement yields a result for $g_{S,T}$ with twice the statistical precision of previous determinations. The g_S result also disfavor the HB χ PT ansatz and more conservative estimate of FVE is essential to obtain reliable prediction on both g_S and g_T . The corresponding g_A result is reserved for a separate publication [20].

TABLE I. Lattice spacing, lattice volume $n_L^3 \times n_T$, pion mass m_π with $m_\pi L$, $m_{\eta_s} \propto \sqrt{m_s}$ and also the number of configurations n_{cfg} .

	$a(\text{fm})$	$n_L^3 \times n_T$	$m_\pi(\text{MeV})$	$m_\pi L$	$m_{\eta_s}(\text{MeV})$	n_{cfg}
C24P34		24×64	341.1(1.8)	4.38	748.61(75)	48
C24P29		24×72	292.7(1.2)	3.75	657.83(64)	190
C32P29		32×64	292.4(1.1)	5.01	658.80(43)	196
C24P23		24×64	230.6(6.7)	2.93	643.93(45)	169
C32P23	0.1053	32×64	228.0(1.2)	3.91	643.93(45)	333
C48P23		48×96	225.6(0.9)	5.79	644.08(62)	54
C48P14		48×96	135.5(1.6)	3.81	706.55(39)	56
C64P14		64×128	134.5(1.6)	4.63	706.55(39)	38
E32P29	0.08973	32×64	286.7(1.8)	4.19	701.37(92)	99
F32P30		32×96	303.2(1.3)	3.56	675.98(97)	91
F48P30		48×96	303.4(0.9)	5.72	674.76(58)	40
F32P21	0.07753	32×64	210.9(2.2)	2.67	658.79(94)	369
F48P21		48×96	207.2(1.1)	3.91	661.94(64)	150
F64P13		64×128	134.1(1.5)	3.37	681.48(59)	46
G36P29	0.06887	36×108	297.2(0.9)	3.73	693.05(46)	43
H48P32	0.05199	48×144	317.2(0.9)	4.00	691.88(65)	46

Simulation Setup: The results in this work, are based on the 2+1 flavor (degenerate up and down quarks plus the strange quark) ensembles [21, 22] from the CLQCD collaboration using the tadpole improved tree level Symanzik (TITLS) gauge action and the tadpole improved tree level Clover (TITLC) fermion action. The information of the ensembles used in this work is summarized in Table I.

The nucleon matrix elements $g_{X=S,T}$ we consider are defined through the relation,

$$\langle N(p, s) | \mathcal{O}_X | N(p, s) \rangle = g_X \bar{u}(p, s) \Gamma_X u(p, s), \quad (1)$$

where the nucleon states $N(p, s)$ and spinors $u(p, s)$ have given momentum p and spin s , $\mathcal{O}_X = \bar{u} \Gamma_X u - \bar{d} \Gamma_X d$ is the iso-vector singlet operator with $\Gamma_S = \mathbf{1}$ and $\Gamma_T = \sigma_{\mu\nu}$.

Within the framework of quantum field theory, the nucleon matrix element is extracted from the ratio of three-point (3pt) to two-point (2pt) correlation functions:

$$\begin{aligned} \mathcal{R}_X(t_f, t; \mathcal{N}) &= \frac{\int d^3x d^3y d^3z \langle \mathcal{N}(\vec{x}, t_f) \mathcal{O}_X(\vec{y}, t) \mathcal{N}^\dagger(\vec{z}, 0) \rangle}{\int d^3x d^3z \langle \mathcal{N}(\vec{x}, t_f) \mathcal{N}^\dagger(\vec{z}, 0) \rangle} \\ &= \langle \mathcal{O}_X \rangle_N + \mathcal{O}(e^{-\delta m t}, e^{-\delta m(t_f - t)}, e^{-\delta m t_f}), \end{aligned} \quad (2)$$

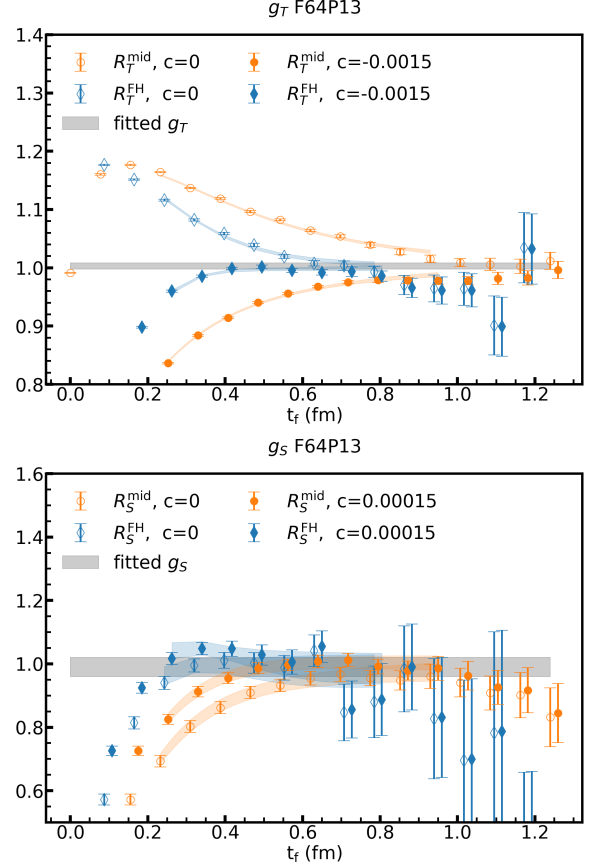


FIG. 1. The dependence of the source-sink separation t_f for the ratios $\mathcal{R}_X^{\text{mid}}(t_f) \equiv \mathcal{R}_X(t_f, t = t_f/2)$ and $\mathcal{R}_X^{\text{FH}}(t_f)$ on the F64P13 ensemble, for the tensor $X = T$ (upper panel) and scalar $X = S$ (lower panel) operator cases. The gray band represents the result from the joint three-state fit. The minimum source-sink separation for fitting is $t_f^{\text{min}} = 3a \sim 0.24$ fm.

where $\mathcal{N}(\vec{x}, t) \equiv \epsilon_{abc} (u_a^T C \gamma_5 d_b) u_c$ denotes the nucleon interpolating operator and δm is the energy gap between the ground state and the first excited state. A significant challenge is that this ratio can suffer from substantial ESC at finite temporal separations t and t_f .

The signal-to-noise ratio of \mathcal{R}_X decays exponentially with t_f , making robust control of excited-state contamination (ESC) contingent upon two factors: high-precision statistical signals at sufficiently large t_f , and the use of proper interpolating field that suppresses contributions from excited states. The recently developed blending method [18, 23] extends the distillation method [24, 25]—which projects the full quark propagators onto their low-energy modes to efficiently suppress ESC—to a stochastic estimation of the full quark propagator itself. The unbiased nature of this method has been rigorously established through both mathematical proof and explicit numerical verification using 2,3,4-point correlation functions [18]. This extension enables the precise calculation of $\mathcal{R}_X(t_f, t)$ for arbitrary combination of t and t_f values

without additional cost for the quark propagator production, thereby generating the high-quality data necessary to investigate possible good choices of the interpolation operators.

As detailed in the supplemental materials [23], our numerical tests indicate that the dominant ESC can be eliminated using a linear combination of matrix elements of \mathcal{O}_X within a basis with two interpolation fields, $H = \{\mathcal{N}, \mathcal{N}_X \equiv \mathcal{N}\mathcal{O}_X\}$ where the second one is “current-involved”, inspired by the discussions in Ref. [11, 19]. The nucleon projection is chosen such that the matrix elements $\langle H_i | \mathcal{O}_X | H_j^\dagger \rangle$ are non-zero for all $i, j = 1, 2$.

Based on the studies using the heavy-than-physical light quark mass [11], Ref. [19] suggested that the ESC of the correlation function $\langle \mathcal{N}_X(t_f) \mathcal{O}_X(t) \mathcal{N}(0) \rangle = V \langle \mathcal{N}(t_f) \mathcal{N}(0) \rangle \langle \mathcal{O}_X(t_f) \mathcal{O}_X(t) \rangle + \mathcal{O}(1)$, which contains a disconnected quark diagram, can be enhanced by the spatial volume V compared to that in the standard three-point function $\langle \mathcal{N}(t_f) \mathcal{O}_X(t) \mathcal{N}(0) \rangle$. This volume-enhanced effect can be the dominant source of ESC, surpassing conventional ones. Consequently, even a small c_X in the improved interpolating field $\mathcal{N} + c_X \mathcal{N}\mathcal{O}_X$ can significantly alter the observed ESC in the extraction of g_X .

In the upper panel of Fig. 1, we show the ratio $\mathcal{R}_T^{\text{mid}} \equiv \mathcal{R}_T(t_f, t_f/2)$ (red dots) and the Feynman-Hellman inspired combination $\mathcal{R}_T^{\text{FH}}(t_f)$ [12] (blue diamonds)

$$\begin{aligned} \mathcal{R}_X^{\text{FH}}(t_f) &\equiv \sum_{t=t_c}^{t_f+a-t_c} \mathcal{R}_X(t_f+a, t) - \sum_{t=t_c}^{t_f-t_c} \mathcal{R}_X(t_f, t) \\ &= \langle \mathcal{O}_X \rangle_N + \mathcal{O}(e^{-\delta m t_f}), \end{aligned} \quad (3)$$

on the physical pion mass ensemble F64P13 at $a = 0.078$ fm, for the distilled interpolation fields \mathcal{N} (hollowed data points) and also $\mathcal{N} + c_T \mathcal{N}_T$ (filled ones) with $c_T = -0.0015$. It is noteworthy that this work marks the first time such high-precision \mathcal{R}_T (and also \mathcal{R}_S) has been obtained directly at the physical pion mass, thanks to the high precision all-to-all propagators using the blending method. This achievement is crucial for suppressing the systematic uncertainty associated with chiral extrapolation.

We do the joint three-state fit to the two- and three-point functions for both interpolating fields, and show the fits with the colored bands which describe the data well, starting from a quite short time separation of $t = 3a \sim 0.24$ fm. The extracted value of g_T is indicated by the gray band, whose uncertainty is comparable to that of the midpoint estimate $\mathcal{R}_X(t_f, t_f/2)$ at $t_f \sim 0.9$ fm. Utilizing the improved interpolating field, which incorporates a small component of the \mathcal{N}_T operator, both ($\mathcal{R}_T^{\text{mid}}$) and ($\mathcal{R}_T^{\text{FH}}$) demonstrate suppression of ESC and exhibit improved convergence toward the ground-state value g_T (gray band) in the fit range shown as the colored bands.

The g_S case is shown in the lower panel of Fig. 1 and shows a similar but minor improvement with $c_0 =$

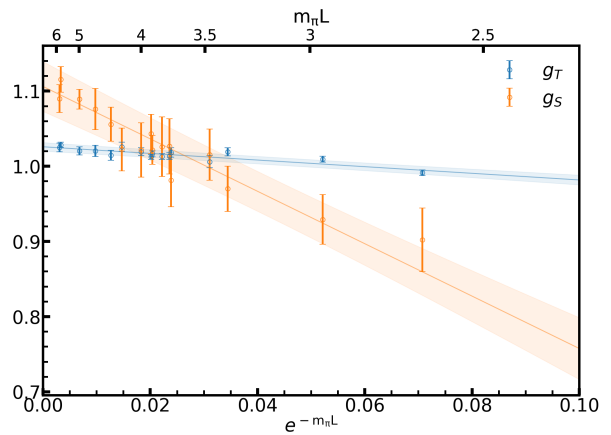


FIG. 2. The finite spatial lattice length L dependence of the g_S and g_T with data points corrected to continuum limit and physical pion mass.

-0.00015 since ESC has been suppressed in the distilled interpolation fields \mathcal{N} well, even though the impact can be more obvious on the other ensembles with heavier pion masses.

We refer the reader to the supplemental materials [23] for an extended discussion on the construction of the interpolation field, including its application to other typical ensembles, as well as a justification for the inefficiency of GEVP with $\mathcal{N}\pi$ states in the current fit range.

Results: To extract the results at the physical point in the continuum and infinite-volume limits, we employ the following joint fit ansatz:

$$\begin{aligned} g_X(a, m_\pi, L) &= g_X^{\text{QCD}} \left(1 + \sum_{i=2,3} c_l^{(i)} (m_\pi^i - m_{\pi, \text{phy}}^i) \right) \\ &\quad (1 + c_V e^{-m_\pi L}) + c_a^{(2)} a^2 + c_a^{(4)} a^4, \end{aligned} \quad (4)$$

where g_X^{QCD} is the target physical value. The parameters c_l , c_V , and c_a describe the pion mass dependence, finite-volume dependence, and discretization effects, respectively. We omit any dependence on the strange quark mass, as our current data lack the sensitivity to constrain such a term.

Our analysis of g_S reveals a strong preference for a phenomenological exponential finite-volume correction, $e^{-m_\pi L}$, over the HB χ PT-predicted form $m_\pi^2 e^{-m_\pi L} / \sqrt{m_\pi L}$ [17]. This is demonstrated by the corrected data (using parameters c_l and c_a from the global fit in Eq. 4), which exhibit a clear linear dependence on $e^{-m_\pi L}$ (orange points, Fig. 2). In contrast, while the FVE for g_T (blue points) is also consistent with a linear $e^{-m_\pi L}$ dependence, it remains statistically compatible with the HB χ PT ansatz due to its smaller overall magnitude.

The pion mass dependence in the continuum and infinite-volume limits is shown in Fig. 3, using similar correction with c_V and c_a obtained from the joint fit with the

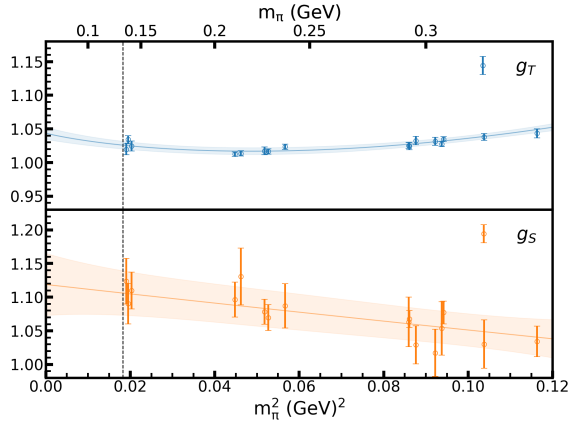


FIG. 3. The pion mass dependence of the g_S and g_T with data points corrected to continuum and infinite volume limits.

ansatz of Eq. 4. The results for both g_T and g_S demonstrate a mild dependence on the pion mass. We incorporate the m_π^3 term to provide an improved description of data at relatively heavy pion masses. The presence of precise results at the physical pion mass for multiple lattice spacings and volumes ensures that the systematic uncertainty originating from the chiral extrapolation remains minor.

The systematic errors associated with infinite volume, continuum and chiral extrapolations are estimated by combining fit models with different fit models using the Akaike Information Criterion (AIC) [4]. The systematic uncertainty from ESC is estimated by taking the difference between the central values obtained from the three-state and two-state fits, and that from the renormalization constant are also integrated through the strategy used in our previous works for the quark masses [21, 22]. The figure for the lattice spacing dependence of the results and also details on the estimate of the systematic uncertainties are provided in the Supplemental Material [23].

Eventually we predict $g_{T,S}^{\text{QCD}}$ with statistical and systematic errors to be:

$$\begin{aligned} g_T^{\text{QCD}} &= 1.0258[79]_{\text{tot}}(56)_{\text{stat}}(24)_a(44)_{\text{FV}}(01)_\chi(24)_{\text{ex}}(05)_{\text{re}}, \\ g_S^{\text{QCD}} &= 1.107[47]_{\text{tot}}(32)_{\text{stat}}(04)_a(29)_{\text{FV}}(01)_\chi(18)_{\text{ex}}(08)_{\text{re}}, \end{aligned} \quad (5)$$

where the mark “stat” denotes the statistical error, while a , FV, χ , ex and “re” represent the systematic errors of the continuum, infinite volume, chiral extrapolation, excited state contamination and renormalization constant, respectively. “tot” is the total error combining the statistical and systematic ones.

In Fig. 4, we compare our results with those from the studies [3, 7, 8, 15, 16, 26–32] that contribute to the current FLAG averages [13]. We achieve a statistical precision for $g_{T/S}$ that is improved by a factor of three or more over all previous works, with the most substantial gains

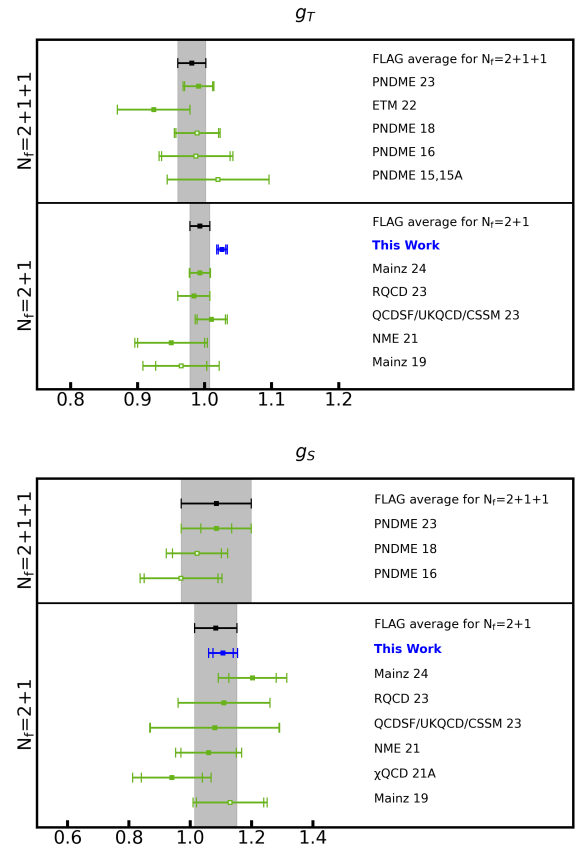


FIG. 4. Comparison of g_T (upper panel) and g_S (lower panel) from this work, PNEME 15 [26, 27]/16 [3]/18 [28]/23 [16], ETM22 [29], Mainz 19 [7]/24 [15], RQCD 23 [8], QCDSF/UUKQCD/CSSM 23 [30], NME 21, [31] χ QCD 21 [32] and also the FLAG averages [13]. There are also lattice calculations [33–37] which are not included by FLAG due to certain uncontrollable systematics. All the values are renormalized at $\overline{\text{MS}}(2 \text{ GeV})$.

on physical-point ensembles. This high precision enables a more robust and conservative evaluation of systematic errors. Our final value has a total uncertainty 1/2 smaller than the previous results.

Using $m_d - m_u = 2.35(12) \text{ MeV}$ —derived from the $N_f = 2 + 1$ FLAG average [13] of m_u/m_d and $m_l = (m_u + m_d)/2$ —and the QED correction $-1.00(7)(14) \text{ MeV}$ from Ref. [4], we predict the neutron-proton mass difference to be:

$$m_n - m_p = 1.60[0.23]_{\text{tot}}(0.11)_{g_S}(0.13)_{\text{ISB}}(0.16)_{\text{QED}} \text{ MeV}. \quad (6)$$

This result is in agreement with the experimental value of 1.293 MeV with 1.3σ . However, employing the newer phenomenological QED correction of $-0.58(16) \text{ MeV}$ [38] yields a prediction roughly 3σ higher than experiment. This discrepancy underscores the importance of an updated direct lattice QCD+QED calculation of the QED correction.

Summary: We report a high-precision calculation of the nucleon isovector scalar (g_S) and tensor (g_T) charges, employing the blending method with current-involved interpolation fields. Our results achieve a significant improvement in precision over the current FLAG averages. Furthermore, they provide robust numerical evidence that the combination of standard and current-involved interpolation fields universally suppresses excited-state contamination (ESC). This suppression is observed to be effective across different current operators, pion masses, volumes, and lattice spacings.

A major strength of the blending method is its capacity to evaluate the efficacy of various interpolation field combinations at arbitrary source-sink separations, without requiring additional propagator generation. The existing propagators produced by this method can, in principle, be used to construct a more complete set of interpolation fields for linear combination of different interpolation operators including the current-involved one, and also generalized eigenvalue problem (GEVP) studies, offering a pathway to further suppress ESC.

Furthermore, our high-precision data reveal a crucial finding: the finite-volume effects (FVEs) for g_S is clearly described by the phenomenological ansatz $e^{-m_\pi L}$. This form is decisively favored over the functional form $m_\pi^2 e^{-m_\pi L} / \sqrt{m_\pi L}$ predicted by HB χ PT. The HB χ PT ansatz is improperly suppressed in the chiral limit, and its use in previous studies would introduced a systematic bias into the extrapolated physical results. We note that our ansatz is consistent with the FVE of the nucleon mass, which scales as $m_\pi^2 e^{-m_\pi L}$ according to the Feynman-Hellmann theorem ($g_{S,q} = \frac{\partial m_N}{\partial m_q}$), and is therefore not unnatural.

Conservative estimate of the FVE systematic uncertainty using the AIC with several ansatz including both

the HB χ PT and also naive $e^{-m_\pi L}$ introduce a systematic uncertainty comparable with the statistical uncertainty. This uncertainty may be universal for a wide range of hadronic matrix elements, including the non-local matrix elements required for parton distribution function (PDF) calculations within the Large Momentum Effective Theory (LaMET) framework [39, 40]. Consequently, previous studies of nucleon matrix elements that used the HB χ PT FVE ansatz may need to reassess this systematic uncertainty.

ACKNOWLEDGMENTS

We thank the CLQCD collaborations for providing us their gauge configurations with dynamical fermions [21], which are generated on HPC Cluster of ITP-CAS, IHEP-CAS and CSNS-CAS, the Southern Nuclear Science Computing Center(SNSC) and the Siyuan-1 cluster supported by the Center for High Performance Computing at Shanghai Jiao Tong University. We thank Rui Zhang for valuable comments and suggestions. The calculations were performed using the PyQUDA package [41] with QUDA [42–44] through HIP programming model [45]. The numerical calculation were carried out on the ORISE Supercomputer, HPC Cluster of ITP-CAS and Advanced Computing East China Sub-center. This work is supported in part by National Key R&D Program of China No.2024YFE0109800, NSFC grants No. 12293060, 12293062, 12525504, 12435002 and 12447101, the science and education integration young faculty project of University of Chinese Academy of Sciences, the Strategic Priority Research Program of Chinese Academy of Sciences, Grant No. XDB34030303 and YSBR-101.

-
- [1] S. Navas *et al.* (Particle Data Group), *Phys. Rev. D* **110**, 030001 (2024).
- [2] T. Bhattacharya, V. Cirigliano, S. D. Cohen, A. Filipuzzi, M. Gonzalez-Alonso, M. L. Graesser, R. Gupta, and H.-W. Lin, *Phys. Rev. D* **85**, 054512 (2012), [arXiv:1110.6448 \[hep-ph\]](#).
- [3] T. Bhattacharya, V. Cirigliano, S. Cohen, R. Gupta, H.-W. Lin, and B. Yoon, *Phys. Rev. D* **94**, 054508 (2016), [arXiv:1606.07049 \[hep-lat\]](#).
- [4] S. Borsanyi *et al.* (BMW), *Science* **347**, 1452 (2015), [arXiv:1406.4088 \[hep-lat\]](#).
- [5] H.-W. Lin, W. Melnitchouk, A. Prokudin, N. Sato, and H. Shows, *Phys. Rev. Lett.* **120**, 152502 (2018), [arXiv:1710.09858 \[hep-ph\]](#).
- [6] F. Yao *et al.* (Lattice Parton), *Phys. Rev. Lett.* **131**, 261901 (2023), [arXiv:2208.08008 \[hep-lat\]](#).
- [7] T. Harris, G. von Hippel, P. Junnarkar, H. B. Meyer, K. Ottnad, J. Wilhelm, H. Wittig, and L. Wrang, *Phys. Rev. D* **100**, 034513 (2019), [arXiv:1905.01291 \[hep-lat\]](#).
- [8] G. S. Bali, S. Collins, S. Heybrock, M. Löffler, R. Rödl, W. Söldner, and S. Weishäupl (RQCD), *Phys. Rev. D* **108**, 034512 (2023), [arXiv:2305.04717 \[hep-lat\]](#).
- [9] C. Alexandrou, G. Koutsou, Y. Li, M. Petschlies, and F. Pittler, *PoS LATTICE2024*, 317 (2025), [arXiv:2412.07263 \[hep-lat\]](#).
- [10] X.-H. Wang, Z.-L. Zhang, X.-H. Cao, C.-L. Fan, X. Feng, Y.-S. Gao, L.-C. Jin, and C. Liu, *Phys. Rev. Lett.* **133**, 141901 (2024), [arXiv:2310.01168 \[hep-lat\]](#).
- [11] L. Barca, G. Bali, and S. Collins, *Phys. Rev. D* **111**, L031505 (2025), [arXiv:2412.13138 \[hep-lat\]](#).
- [12] C. C. Chang *et al.*, *Nature* **558**, 91 (2018), [arXiv:1805.12130 \[hep-lat\]](#).
- [13] Y. Aoki *et al.* (Flavour Lattice Averaging Group (FLAG)), (2024), [arXiv:2411.04268 \[hep-lat\]](#).
- [14] V. Cirigliano, J. de Vries, L. Hayen, E. Mereghetti, and A. Walker-Loud, *Phys. Rev. Lett.* **129**, 121801 (2022), [arXiv:2202.10439 \[nucl-th\]](#).
- [15] C. Alexandrou, M. Constantinou, S. Dinter, V. Drach, K. Jansen, C. Kallidonis, and G. Koutsou, *Phys. Rev. D* **88**, 014509 (2013), [arXiv:1303.5979 \[hep-lat\]](#).
- [16] Y.-C. Jang, R. Gupta, T. Bhattacharya, B. Yoon, and H.-W. Lin (Precision Neutron Decay Matrix Ele-

- ments (PNDME)), *Phys. Rev. D* **109**, 014503 (2024), [arXiv:2305.11330 \[hep-lat\]](#).
- [17] S. R. Beane and M. J. Savage, *Phys. Rev. D* **70**, 074029 (2004), [arXiv:hep-ph/0404131](#).
- [18] Z.-C. Hu, J.-H. Wang, X. Jiang, L. Liu, S.-H. Su, P. Sun, and Y.-B. Yang, (2025), [arXiv:2505.01719 \[hep-lat\]](#).
- [19] L. Barca, (2025), [arXiv:2508.09006 \[hep-lat\]](#).
- [20] In preparation..
- [21] Z.-C. Hu *et al.* (CLQCD), *Phys. Rev. D* **109**, 054507 (2024), [arXiv:2310.00814 \[hep-lat\]](#).
- [22] H.-Y. Du *et al.* (CLQCD), *Phys. Rev. D* **111**, 054504 (2025), [arXiv:2408.03548 \[hep-lat\]](#).
- [23] Supplemental materials.
- [24] M. Peardon, J. Bulava, J. Foley, C. Morningstar, J. Dudek, R. G. Edwards, B. Joo, H.-W. Lin, D. G. Richards, and K. J. Juge (Hadron Spectrum), *Phys. Rev. D* **80**, 054506 (2009), [arXiv:0905.2160 \[hep-lat\]](#).
- [25] C. Morningstar, J. Bulava, J. Foley, K. J. Juge, D. Lenkner, M. Peardon, and C. H. Wong, *Phys. Rev. D* **83**, 114505 (2011), [arXiv:1104.3870 \[hep-lat\]](#).
- [26] [PNDME 15] T. Bhattacharya, V. Cirigliano, R. Gupta, H.-W. Lin, and B. Yoon, *Phys. Rev. Lett.* **115**, 212002 (2015), [arXiv:1506.04196 \[hep-lat\]](#).
- [27] [PNDME 15A] T. Bhattacharya, V. Cirigliano, S. Cohen, R. Gupta, A. Joseph, H.-W. Lin, and B. Yoon, *Phys. Rev. D* **92**, 094511 (2015), [arXiv:1506.06411 \[hep-lat\]](#).
- [28] [PNDME 18] R. Gupta, Y.-C. Jang, B. Yoon, H.-W. Lin, V. Cirigliano, and T. Bhattacharya, *Phys. Rev. D* **98**, 034503 (2018), [arXiv:1806.09006 \[hep-lat\]](#).
- [29] [ETM 22] C. Alexandrou *et al.*, *Phys. Rev. D* **107**, 054504 (2023), [arXiv:2202.09871 \[hep-lat\]](#).
- [30] [QCDSF/UKQCD/CSSM 23] R. E. Smail *et al.*, *Phys. Rev. D* **108**, 094511 (2023), [arXiv:2304.02866 \[hep-lat\]](#).
- [31] [NME 21] S. Park, R. Gupta, B. Yoon, S. Mondal, T. Bhattacharya, Y.-C. Jang, B. Joó, and F. Winter, *Phys. Rev. D* **105**, 054505 (2022), [arXiv:2103.05599 \[hep-lat\]](#).
- [32] [χ QCD 21A] L. Liu, T. Chen, T. Draper, J. Liang, K.-F. Liu, G. Wang, and Y.-B. Yang, *Phys. Rev. D* **104**, 094503 (2021), [arXiv:2103.12933 \[hep-lat\]](#).
- [33] [JLQCD 18] N. Yamanaka, S. Hashimoto, T. Kaneko, and H. Ohki, *Phys. Rev. D* **98**, 054516 (2018), [arXiv:1805.10507 \[hep-lat\]](#).
- [34] [LHPC 19] N. Hasan, J. Green, S. Meinel, M. Engelhardt, S. Krieg, J. Negele, A. Pochinsky, and S. Syritsyn, *Phys. Rev. D* **99**, 114505 (2019), [arXiv:1903.06487 \[hep-lat\]](#).
- [35] [RBC/UKQCD 19] M. Abramczyk, T. Blum, T. Izubuchi, C. Jung, M. Lin, A. Lytle, S. Ohta, and E. Shintani, *Phys. Rev. D* **101**, 034510 (2020), [arXiv:1911.03524 \[hep-lat\]](#).
- [36] [PACS 22B] R. Tsuji, N. Tsukamoto, Y. Aoki, K.-I. Ishikawa, Y. Kuramashi, S. Sasaki, E. Shintani, and T. Yamazaki, *Phys. Rev. D* **106**, 094505 (2022), [arXiv:2207.11914 \[hep-lat\]](#).
- [37] [ETM 19] C. Alexandrou, S. Bacchio, M. Constantinou, J. Finkenrath, K. Hadjiyiannakou, K. Jansen, G. Koutsou, and A. Vaquero Aviles-Casco, *Phys. Rev. D* **102**, 054517 (2020), [arXiv:1909.00485 \[hep-lat\]](#).
- [38] J. Gasser, H. Leutwyler, and A. Rusetsky, *Phys. Lett. B* **814**, 136087 (2021), [arXiv:2003.13612 \[hep-ph\]](#).
- [39] X. Ji, *Phys. Rev. Lett.* **110**, 262002 (2013), [arXiv:1305.1539 \[hep-ph\]](#).
- [40] X. Ji, Y.-S. Liu, Y. Liu, J.-H. Zhang, and Y. Zhao, *Rev. Mod. Phys.* **93**, 035005 (2021), [arXiv:2004.03543 \[hep-ph\]](#).
- [41] X. Jiang, C. Shi, Y. Chen, M. Gong, and Y.-B. Yang, (2024), [arXiv:2411.08461 \[hep-lat\]](#).
- [42] M. A. Clark, R. Babich, K. Barros, R. C. Brower, and C. Rebbi, *Comput. Phys. Commun.* **181**, 1517 (2010), [arXiv:0911.3191 \[hep-lat\]](#).
- [43] R. Babich, M. A. Clark, B. Joo, G. Shi, R. C. Brower, and S. Gottlieb, in *SC11 International Conference for High Performance Computing, Networking, Storage and Analysis Seattle, Washington, November 12-18, 2011* (2011) [arXiv:1109.2935 \[hep-lat\]](#).
- [44] M. A. Clark, B. Jo, A. Strelchenko, M. Cheng, A. Gambhir, and R. Brower, (2016), [arXiv:1612.07873 \[hep-lat\]](#).
- [45] Y.-J. Bi, Y. Xiao, M. Gong, W.-Y. Guo, P. Sun, S. Xu, and Y.-B. Yang, *Proceedings, 37th International Symposium on Lattice Field Theory (Lattice 2019): Wuhan, China, June 16-22 2019*, PoS **LATTICE2019**, 286 (2020), [arXiv:2001.05706 \[hep-lat\]](#).
- [46] M. Lüscher and U. Wolff, *Nucl. Phys. B* **339**, 222 (1990).
- [47] B. Blossier, M. Della Morte, G. von Hippel, T. Mendes, and R. Sommer, *JHEP* **04**, 094 (2009), [arXiv:0902.1265 \[hep-lat\]](#).
- [48] L. Barca, G. Bali, and S. Collins, *Phys. Rev. D* **107**, L051505 (2023), [arXiv:2211.12278 \[hep-lat\]](#).
- [49] A. V. Grebe and M. Wagman, PoS **LATTICE2023**, 049 (2024), [arXiv:2312.00321 \[hep-lat\]](#).
- [50] C. Alexandrou, G. Koutsou, Y. Li, M. Petschlies, and F. Pittler, *Phys. Rev. D* **110**, 094514 (2024), [arXiv:2408.03893 \[hep-lat\]](#).
- [51] A. Hackl and C. Lehner, (2024), [arXiv:2412.17442 \[hep-lat\]](#).
- [52] Y.-S. Gao, Z.-L. Zhang, X. Feng, L.-C. Jin, C. Liu, and U.-G. Meißner, *Phys. Rev. Lett.* **134**, 171904 (2025), [arXiv:2502.12074 \[hep-lat\]](#).
- [53] S. Prelovsek, U. Skerbis, and C. B. Lang, *JHEP* **01**, 129 (2017), [arXiv:1607.06738 \[hep-lat\]](#).
- [54] W. Detmold, W. I. Jay, G. Kanwar, P. E. Shanahan, and M. L. Wagman, *Phys. Rev. D* **109**, 094516 (2024), [arXiv:2403.00672 \[hep-lat\]](#).
- [55] S. Borsanyi *et al.*, *Nature* **593**, 51 (2021), [arXiv:2002.12347 \[hep-lat\]](#).

SUPPLEMENTAL MATERIALS

A. Brief review of the blending method

The blending method [18] splits the vector space associated with the lattice sites and color degrees of freedom, with dimension $[\mathcal{L}] = N_c N_L^3$ into two subspaces:

1. Subspace \mathcal{L}_1 (that used in the distillation method [24]): The span of the N_e low-lying eigenvectors $\{v_{\lambda_i}\}_{i=1}^{N_e}$ of the discrete Laplace operator;
2. Complement subspace \mathcal{L}_2 : The orthogonal complement of \mathcal{L}_1 in \mathcal{L} , i.e., $\mathcal{L}_2 = \mathcal{L}/\mathcal{L}_1$, with dimension $[\mathcal{L}_2] = N_c N_L^3 - N_e$.

A ‘‘blending space’’ is constructed by combining the eigenvectors $\{\phi_i \equiv v_{\lambda_i}\}_{i=1}^{N_e}$ spanning \mathcal{L}_1 , and a set of N_{st} orthogonal random vectors $\{\phi_{N_e+j} \equiv \eta_j\}_{j=1}^{N_{st}}$ sampled uniformly from \mathcal{L}_2 . Then the identity operator \hat{I} on \mathcal{L} can be unbiasedly approximated as:

$$\hat{I} = \sum_{i=1}^{[\mathcal{L}]} |V_i\rangle\langle V_i| = \lim_{N_{st} \rightarrow [\mathcal{L}_2]} \sum_{k=1}^{N_e + N_{st}} \Omega_k^{(1)} |\phi_k\rangle\langle\phi_k|, \quad \Omega_k^{(1)} = \begin{cases} 1 & \text{for } k \leq N_e, \\ [\mathcal{L}_2]/N_{st} & \text{for } k > N_e, \end{cases} \quad (7)$$

where $\{|V_i\rangle\}$ is a complete orthonormal basis of \mathcal{L} . Then the all-to-all propagator S can be projected onto the blending space,

$$S_{ij}(t_1, t_2) = \int d^3x d^3y \langle \phi_i(\vec{x}, t_1) | S(\vec{x}, t_1; \vec{y}, t_2) | \phi_j(\vec{y}, t_2) \rangle, \quad (8)$$

and then compressed from $(4N_c N_T N_L^3)^2$ to $(4N_T(N_e + N_{st}))^2$ (projected propagator) + $N_T N_c N_L^3(N_e + N_{st})$ (vectors in the blending space).

More details about the mathematical proof and numerical justification of the blending method can be found in Ref. [18].

B. Excited state contamination

1. Brief review of GEVP

The extraction of the ground-state matrix element from lattice calculations is systematically affected by excited-state contamination (ESC). The standard ratio computed at finite t_f , t and given interpolation operator \mathcal{N} is defined as,

$$\begin{aligned} \mathcal{R}_X(t_f, t; \mathcal{N}) &= \frac{\int d^3x d^3y d^3z \langle \mathcal{N}(\vec{x}, t_f) \mathcal{O}_X(\vec{y}, t) \mathcal{N}^\dagger(\vec{z}, 0) \rangle}{\int d^3x d^3z \langle \mathcal{N}(\vec{x}, t_f) \mathcal{N}^\dagger(\vec{z}, 0) \rangle} \\ &= \langle \mathcal{O}_X \rangle_N + \mathcal{O}(e^{-\delta m t}, e^{-\delta m(t_f - t)}, e^{-\delta m t_f}). \end{aligned} \quad (9)$$

The leading ESCs include terms of order $e^{-\delta m t}$ and $e^{-\delta m(t_f - t)}$ which originate from transitions between the ground state and excited states with mass gap δm , and also terms of order $e^{-\delta m t_f}$ which arise from matrix elements of \mathcal{O}_X within the excited states themselves.

Since different hadron interpolation operators have different overlap with ground and excited states, the generalized eigenvalue problem (GEVP) provides a framework to suppress the low energy excited states through the combination of different interpolation operators [46, 47]. Under GEVP, one introduces a tower of interpolation operators (GEVP basis),

$$\{\mathcal{O}_0, \mathcal{O}_1, \mathcal{O}_2, \dots, \mathcal{O}_{N-1}\}. \quad (10)$$

Those interpolation operators furnish a matrix of two-point functions (2pts),

$$C_{i,j}(t) = \langle \mathcal{O}_i(t) \mathcal{O}_j^\dagger(0) \rangle. \quad (11)$$

Since $C_{i,j}(t)$ is the transfer matrix e^{-Ht} of the QCD Hamiltonian in a truncated Hilbert space, its eigenstates are also approximations to the corresponding hadrons. Since the GEVP basis may not be orthonormal, one needs to solve a GEVP in order to find the eigenstates,

$$C_{i,j}(t') V_j^\alpha(t', t_0) = C_{i,j}(t_0) V_j^\alpha(t', t_0) \lambda^\alpha(t', t_0), \quad (12)$$

where $V_j^\alpha(t', t_0)$ and $\lambda^\alpha(t', t_0)$ are the α -th eigenstate and eigenvalue, respectively. By analyzing $\lambda^\alpha(t', t_0)$, one can find the energy of each eigenstate, where the ground state is labeled as $V_j^0(t', t_0)$. The optimized ground state hadron interpolation operator can be constructed as,

$$\mathcal{O}^{\text{opt}}(t', t_0) = \sum_{j=0}^{N-1} V_j^{0*}(t', t_0) \mathcal{O}_j . \quad (13)$$

Then, this optimized operator can be utilized to calculate the matrix element. As shown in Ref. [47], under proper choices of time slices, the ESC for the three-point functions behaves as $O(e^{-\delta m' t_0})$, where $\delta m' = m_N - m_0$ is an enlarged energy gap compared to ordinary methods with a single interpolation operator in Eq. (9). Therefore, GEVP is a large time asymptotic analysis, which systematically approaches the desired ground state with an increased number of interpolation operators.

But the question is how to choose an efficient GEVP basis for a desired matrix element. From the point of view of large time asymptotic analysis, one should start from the lowest energy states and gradually approaches the higher energy states, in the subspace constrained by the quantum number of hadron interpolation operator. Therefore, the operator list should start, from the operators trying to capture the lowest energy states, to higher ones. For example, for nucleon matrix elements, one should start from N , $N\pi$, $N\pi\pi$, $N\sigma$ and so on. Recent works have explored the ESC for nucleon matrix elements under GEVP [11, 48–52].

2. current-involved excited state contamination

The concept of current-meson dominance, introduced in Refs. [11, 19], posits that certain excited states are selectively enhanced by the inserted current, becoming the dominant source of contamination in the desired matrix element. Specifically, the energy gap for this dominant state is $\Delta E = m_X$, where m_X is the mass of the ground state projected by the current operator O_X . Conventional nucleon interpolation operators are inefficient at isolating this particular contamination. The solution is to include the current-involved operator $\mathcal{N}_X(\vec{0}) \equiv \mathcal{N}(\vec{0}) \sum_{\vec{z}} O_X(\vec{z})$, where $\mathcal{N} = \epsilon_{abc} u_a C \gamma_5 d_b u_c$ is the standard proton interpolating field.

Consider the correlation function of $\mathcal{N}(t_f)$ and $\mathcal{N}_X(0)$ with an inserted current $O_X(t)$, it can be decomposed into the quark line disconnected and connected diagrams,

$$\begin{aligned} \sum_{\vec{x}, \vec{y}} \langle \mathcal{N}(t_f; \vec{x}) O_X(t; \vec{0}) \mathcal{N}_X^\dagger(0; \vec{y}) \rangle &= V \sum_y \langle \mathcal{N}(t_f; \vec{0}) \mathcal{N}^\dagger(0; \vec{y}) \rangle \sum_z \langle O_X(t; \vec{0}) O_X^\dagger(0; \vec{z}) \rangle \\ &\quad + \text{quark connected diagrams} \\ &= \mathcal{O}(V e^{-m_N t_f} e^{-m_X t}) + \text{quark connected diagrams} \end{aligned} \quad (14)$$

where the first term in the right hand side corresponds to the ESC we need and is enhanced by a spatial volume factor V . This significant enhancement underscores why the \mathcal{N}_X operator must be included in the basis.

Here, we provide another argument by studying the “linear error correction” to a nucleon matrix element. Denote the true nucleon state as $|N\rangle$ and the estimated nucleon state as $|N^{\text{est}}\rangle$. Suppose they differ by a perturbation $|\delta N\rangle$ caused by ESC,

$$|N^{\text{est}}\rangle = |N\rangle + |\delta N\rangle . \quad (15)$$

One calculates the matrix element using the estimated nucleon state,

$$\langle N^{\text{est}} | O_X | N^{\text{est}} \rangle = \langle N | O_X | N \rangle + \langle \delta N | O_X | N \rangle + \langle N | O_X | \delta N \rangle + \langle \delta N | O_X | \delta N \rangle , \quad (16)$$

which differs from the true nucleon matrix element $\langle N | O_X | N \rangle$ by linear and quadratic error corrections. We focus on the linear error correction $\langle N | O_X | \delta N \rangle$ or $\langle \delta N | O_X | N \rangle$ and ignore the quadratic correction. $|\delta N\rangle$ is a vector in Hilbert space that could point towards various possible directions. However, only the direction parallel to $O_X | N \rangle$ contributes to the linear error correction while the orthogonal directions vanish. Thus the second interpolation operator \mathcal{N}_X should be a good choice to mimic this direction.

In this work, we follow this idea to choose a two-operator basis as a preliminary investigation in this direction,

$$H_X = \{ \mathcal{N}, \mathcal{N}_X \} , \quad (17)$$

and then the basis of the scalar charge case differs from the tensor one. For O_S , the proton is an unpolarized state; but for O_T with $\epsilon^{ijk} \sigma_{ij}$, the proton is polarized along the k -direction so that \mathcal{N}_T has the same polarization as \mathcal{N} . Since

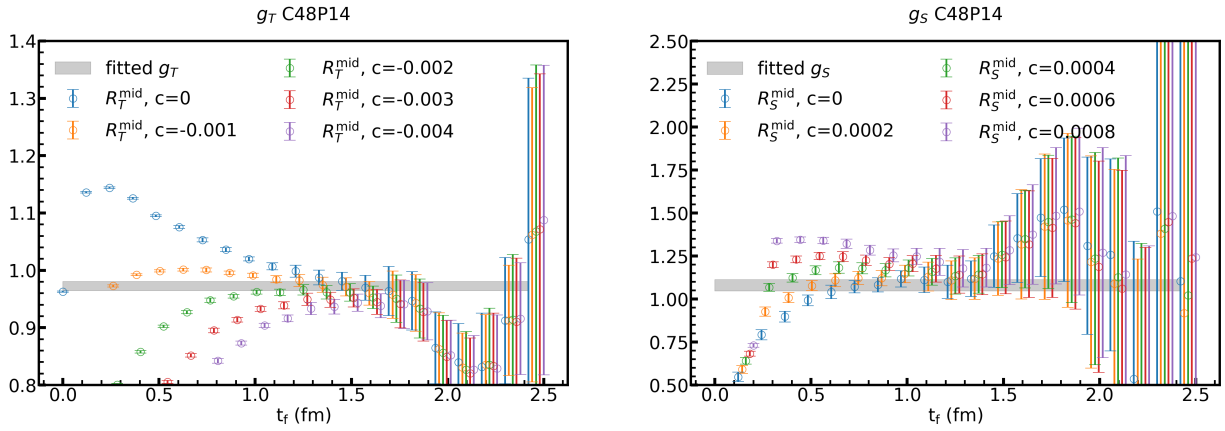


FIG. 5. The dependence of the source-sink separation t_f for the ratios $\mathcal{R}_X^{\text{mid}}(t_f, \mathcal{N}(c)) \equiv \mathcal{R}_X(t_f, t = t_f/2; \mathcal{N}(c))$ under various coefficients c , for the iso-vector tensor charge (left panel) and scalar charge (right panel). Those ratios are generated on C48P14 with physical pion mass and $a = 0.105$ fm and renormalized to $\overline{\text{MS}}(2 \text{ GeV})$

O_S and O_T are parity even operators, we consider the S-wave type scattering state and the momentum projections for all the operators are zero.

Then the optimal operator which can suppress the current-involved ESC can be expressed as a linear combination $\mathcal{N}^{\text{opt}} = \mathcal{N} + c^{\text{opt}} \mathcal{N}_X$ with the coefficient c to be determined. In our calculation, we use the interpolation operator \mathcal{N}_X directly and not to project the reducible lattice representations onto the spin-1/2, isospin-1/2 subspace to obtain irreducible operators [53, 54]. With our choice \mathcal{N}_X , excitations with higher spin or isospin are allowed and are handled effectively by varying the coefficient c in the linear combination. In particular, both \mathcal{N}_S and \mathcal{N}_T also create isospin-3/2 states, which share the same energy with isospin-1/2 states because we take $m_u = m_d$. Moreover, \mathcal{N}_T couples to both spin-1/2 and spin-3/2 $N b_1$ states; these correspond to different linear combinations of polarization components but are degenerate eigenstates of the Hamiltonian. Consequently, such higher-spin or higher-isospin excited states share the same Euclidean-time dependence in the linear error correction and can be absorbed by a rescaling of c .

We present the midpoint ratio $\mathcal{R}_X^{\text{mid}}(t_f; c) \equiv \mathcal{R}_X(t_f, t_f/2; \mathcal{N}(c))$ on one of the physical pion mass ensembles, C48P14 ($a = 0.105$ fm), in Fig. 5, exploring its dependence on the source-sink separation t_f/a and the parameter c in the interpolation operator combination $\mathcal{N}(c) \equiv \mathcal{N} + c \mathcal{N}_X$. The data show a strong c -dependence at small t_f for both charges, despite converging to a common ground-state value (gray band) at large t_f . A notable finding is that the optimal c values for good ESC suppression are very small—approximately -0.001 (tensor) and 0.0004 (scalar). Consequently, determining these small coefficients via a standard GEVP analysis in the H_X basis is plagued by large relative uncertainties.

On each ensemble, we can find an optimized coefficient $c = c^{\text{opt}}$ with mild time-dependencies in $R_X^{\text{mid}}(t_f)$ and $R_X^{\text{FH}}(t_f)$ in moderate and large t_f . Fig. 6 displays the results for the tensor charge g_T on four characteristic ensembles covering different pion masses (including the physical pion mass), volumes, and lattice spacings:

- 1) C48P23 with $a=0.105$ fm, $m_\pi \sim 230$ MeV, $L \sim 5.1$ fm (upper left panel);
- 2) C32P23 with $a=0.105$ fm, $m_\pi \sim 230$ MeV, $L \sim 3.4$ fm (upper right panel);
- 3) C48P23 with $a=0.105$ fm, $m_\pi \sim 135$ MeV, $L \sim 5.1$ fm (lower left panel);
- 4) F48P21 with $a=0.077$ fm, $m_\pi \sim 210$ MeV, $L \sim 3.7$ fm (lower right panel);

To illustrate the ESC, we also define another characteristic functions

$$\mathcal{R}_X^{\text{FH}}(t_f) \equiv \sum_{t=t_c}^{t_f+a-t_c} \mathcal{R}_X(t_f+a, t) - \sum_{t=t_c}^{t_f-t_c} \mathcal{R}_X(t_f, t) = \langle \mathcal{O}_X \rangle_N + \mathcal{O}(e^{-\delta m t_f}), \quad (18)$$

which have different ESC compared to $\mathcal{R}_T^{\text{mid}} = \langle \mathcal{O}_X \rangle_N + \mathcal{O}(e^{-\delta m t_f/2})$. Among all of them, the ESCs of both $\mathcal{R}_X^{\text{mid}}$ and $\mathcal{R}_X^{\text{FH}}$ are dramatically suppressed after an optimized coefficient $c = c_X$ is chosen compared to the $c = 0$ case.

Similar improvements are observed for the scalar charge as shown in Fig. 7, except for C48P23 where the ESCs have been already efficiently suppressed with the distilled interpolation fields. Notably, the optimal parameter c_X^{opt} is consistently small across all cases examined, for both the tensor ($X = T$) and scalar ($X = S$) charges. However, a direct comparison of its values across ensembles is complicated by the fact that the distillation interpolation fields utilize different upper eigenvalue bands of the Laplace operator in each case. A systematic investigation into the lattice spacing, pion mass, and volume dependence of c^{opt} is therefore reserved for future study.

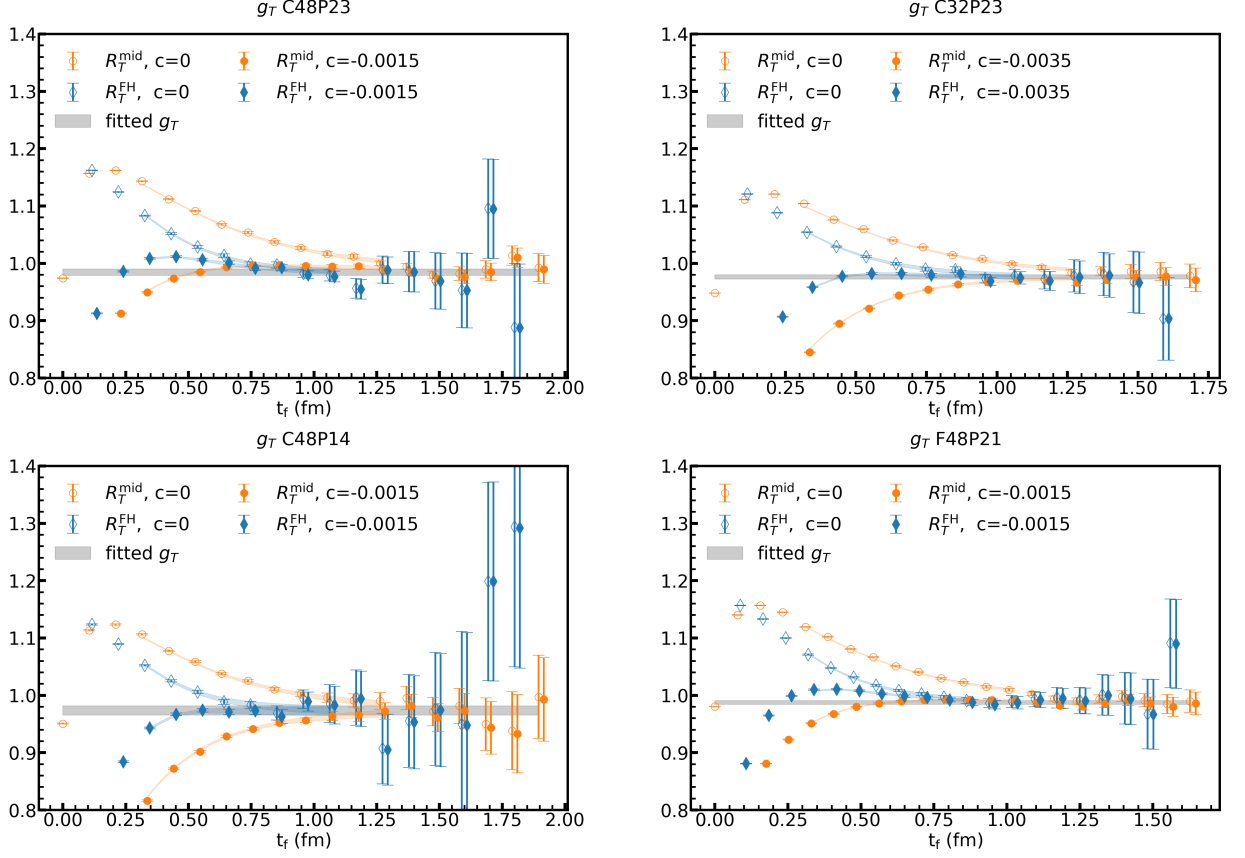


FIG. 6. The dependence of the source-sink separation t_f for the ratios $\mathcal{R}_X^{\text{mid}}(t_f, c) \equiv \mathcal{R}_X(t_f, t = t_f/2; \mathcal{N}(c))$ and Feynman-Hellman functions $\mathcal{R}_X^{\text{FH}}(t_f)$ for the tensor charge $X = T$ on various ensembles: C48P23 (upper left), C32P23 (upper right), C48P14 (lower left), F48P21 (lower right), which cover different pion masses, volumes, and lattice spacings. The gray band represents the result from the joint three-state fit. The minimum source-sink separation for fitting is $t_f^{\text{min}} \sim 0.3$ fm.

To obtain the ground state matrix element, we perform a joint fit combining $c = 0$ and $c = c^{\text{opt}}$ (the one with good suppression of ESC) with respect to t and t_f dependencies in $\mathcal{R}_X(t_f, t; \mathcal{N}(c))$ and $c_2(t_f; \mathcal{N}(c))$ with $c_2(t_f; \mathcal{N}) \equiv \int d^3x d^3z \langle \mathcal{N}(\vec{x}, t_f) \mathcal{N}^\dagger(\vec{z}, 0) \rangle$, using a three-state parametrization (one ground state and two excited states),

$$\begin{aligned}
 c_2(t_f; c) &= [1 + d_1^2(c)e^{-\Delta_1 t_f} + d_2^2(c)e^{-\Delta_2 t_f}] Z(c) e^{-m_0 t_f}, \\
 \mathcal{R}_X(t_f, t; c) &= [b_{00} + b_{10} d_1(c)(e^{-\Delta_1 t} + e^{-\Delta_1(t_f-t)}) + b_{20} d_2(c)(e^{-\Delta_2 t} + e^{-\Delta_2(t_f-t)}) \\
 &\quad + b_{11} d_1^2(c) e^{-\Delta_1 t_f} + b_{12} d_1(c) d_2(c) (e^{-\Delta_1(t_f-t) - \Delta_2 t} + e^{-\Delta_2(t_f-t) - \Delta_1 t}) + b_{22} d_2^2(c) e^{-\Delta_2 t_f}] \\
 &\quad / [1 + d_1^2(c) e^{-\Delta_1 t_f} + d_2^2(c) e^{-\Delta_2 t_f}], \tag{19}
 \end{aligned}$$

where $\Delta_i = m_i - m_0$ denotes the mass difference between excited state i and the ground state. The b_{ij} denotes the matrix element from state i to state j , where b_{00} is the ground state matrix element of interest. The values m_0 , Δ_i , and b_{ij} are independent of c , while the coefficients $Z(c)$ and $d_i(c)$ differ between the cases $c = 0$ and $c = c^{\text{opt}}$. The fitted ground state matrix elements are shown as the gray bands in Figs. 6 and 7.

We expect the fitted ground-state matrix elements to be stable under variations of c_X around its optimized value. The theoretical basis for this is that an interpolator with an arbitrary c can be expressed as a linear combination of the $c = 0$ and $c = c^{\text{opt}}$ cases, with corrections only at $\mathcal{O}(c^2)$. This stability is confirmed numerically in Fig. 8 and 9, which compares $\mathcal{R}_X^{\text{mid}/\text{FH}}$ for $c = c^{\text{opt}}$ and $c = 2c^{\text{opt}}$. The joint fits yield consistent ground-state matrix elements in both cases, validating the robustness of our extraction.

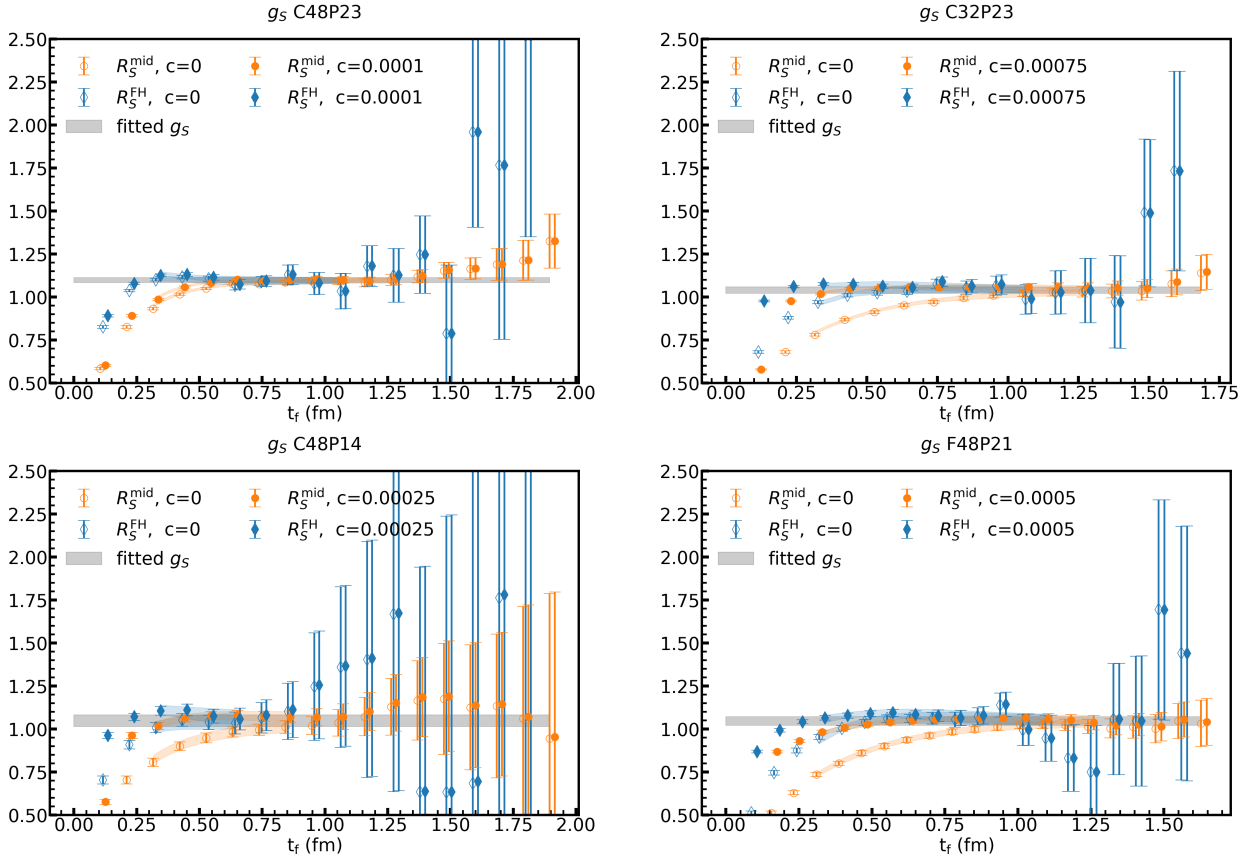


FIG. 7. Similar to Fig. 6 except for the scalar charge.

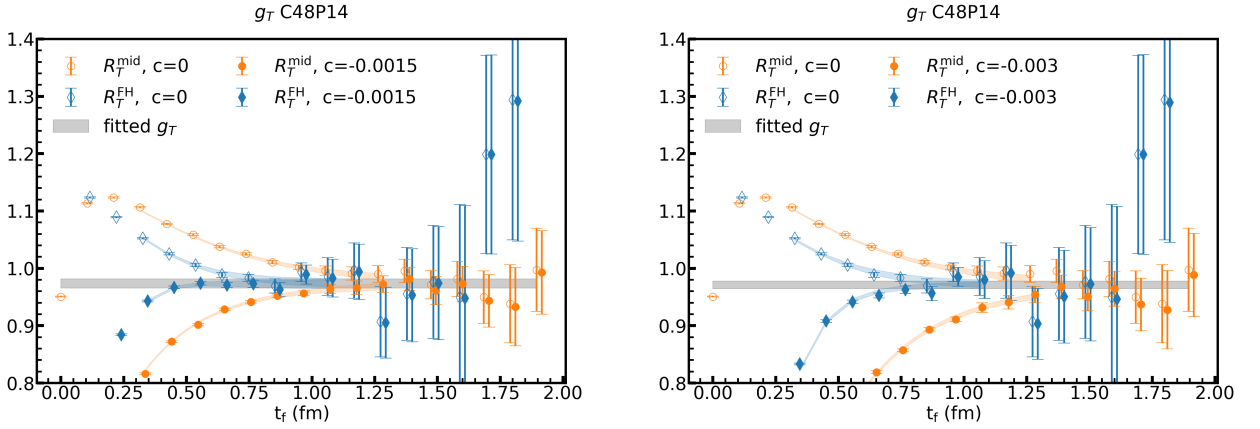


FIG. 8. The dependence of the source-sink separation t_f for the ratios $\mathcal{R}_X^{\text{mid}}(t_f) \equiv \mathcal{R}_X(t_f, t = t_f/2)$ and Feynman-Hellman functions $\mathcal{R}_X^{\text{FH}}(t_f)$ for the tensor charges on C48P14, with chosen c^{opt} (left panel) and $2c^{\text{opt}}$ (right panels). The ground-state matrix elements from the joint three-state fit (gray bands) agree with each other.

3. Influence from $N\pi$

We also test the influence from the nucleon-pion scattering state [48–50] using a two-operator GEVP basis, $\{\mathcal{N}, \mathcal{N}\pi\}$. The optimized linear combination is obtained by solving Eq. (12), where the stabilized solutions can be obtained at relatively large t' and t_0 . As tested on C48P14 and shown in Fig. 10, the results with and without GEVP have similar time dependencies in moderate and large t_f , indicating that the nucleon-pion scattering state has a smaller influence on the ESC for both g_T and g_S , compared to the current-enhanced excited states. Therefore, $\mathcal{N}\pi$ is not considered

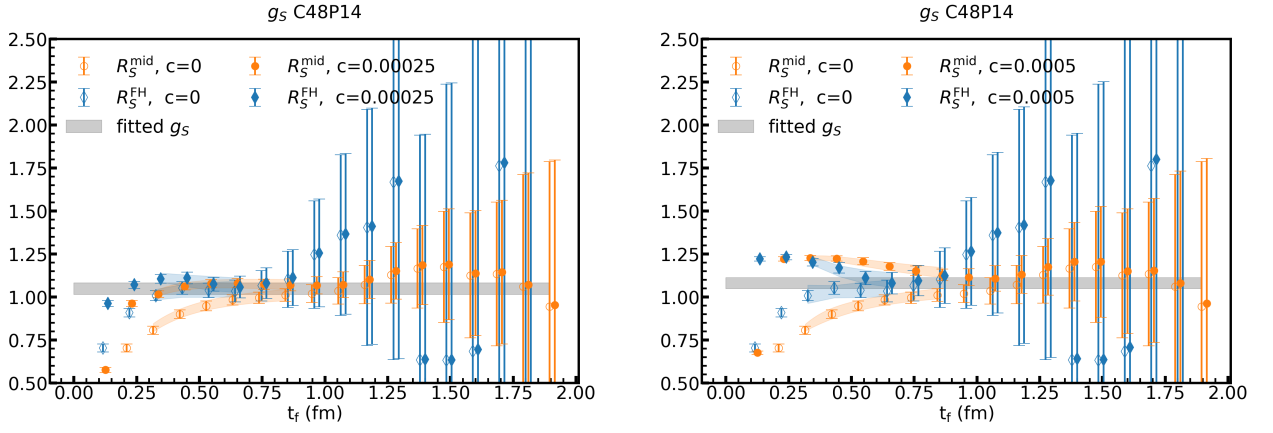


FIG. 9. Similar to Fig. 8 except for the scalar charge.

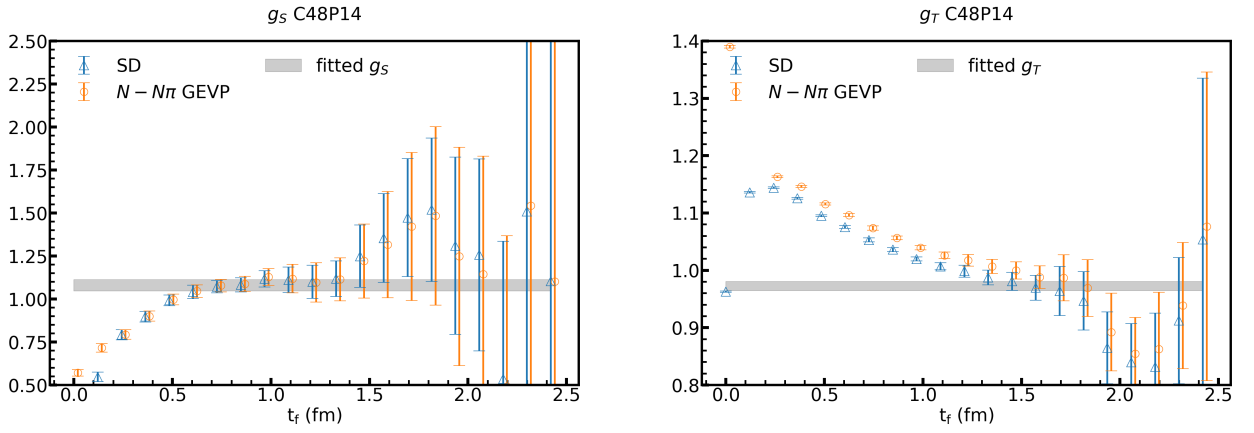


FIG. 10. The comparison between the $\mathcal{N} - \mathcal{N}\pi$ GEVP (orange circles) and standard (SD, blue triangles) \mathcal{N} interpolation operator on $\mathcal{R}_X^{\text{mid}}(t_f) \equiv \mathcal{R}_X(t_f, t = t_f/2)$. The left panel displays the tensor charge as a function of the sink source separation t_f . The right panel is for scalar charge. The lattice data are generated on C48P14 (physical pion mass).

in extracting the ground state matrix elements in our calculations.

TABLE II. The g_S and g_T values from 2-state fit and 3-state fit for comparison.

	N_e	N_{st}	$g_S^{2\text{-state}}$	$g_S^{3\text{-state}}$	$g_T^{2\text{-state}}$	$g_T^{3\text{-state}}$
C24P34	50	250	1.026(18)	1.025(23)	1.0055(57)	1.0040(66)
C24P29	50	50	0.932(19)	1.017(37)	0.9838(36)	0.9810(45)
C32P29	60	60	1.113(13)	1.077(13)	0.9971(20)	0.9879(55)
C24P23	50	50	0.935(44)	0.942(33)	0.9661(40)	0.9670(39)
C32P23	60	60	0.937(28)	1.033(19)	0.9816(37)	0.9739(38)
C48P23	100	200	1.108(19)	1.100(18)	0.9949(36)	0.9822(58)
C48P14	150	200	1.040(35)	1.048(34)	0.9756(69)	0.9723(81)
C64P14	150	50	1.097(25)	1.108(27)	0.9846(85)	0.9865(75)
E32P29	50	50	1.037(30)	1.004(28)	1.0035(45)	1.0017(63)
F32P30	100	200	0.943(24)	0.997(40)	0.9990(28)	0.9994(37)
F48P30	100	200	1.117(15)	1.084(17)	1.0210(24)	1.0151(35)
F32P21	50	50	0.897(34)	0.906(42)	0.9643(55)	0.9644(38)
F48P21	100	60	1.005(19)	1.045(26)	0.9910(26)	0.9855(33)
F64P13	140	60	0.959(28)	0.988(30)	0.9853(79)	1.0009(54)
G36P29	60	140	0.967(32)	0.951(35)	1.0088(60)	1.0066(61)
H48P32	100	200	0.963(28)	0.977(36)	1.0201(47)	1.0217(53)
$g_{S/T}^{\text{physical}}$			1.125(29)	1.107(32)	1.0234(54)	1.0174(64)

C. Systematic uncertainties

Using the current-involved interpolation field combination discussed previously, we conducted a systematic analysis employing both two-state and three-state fits. To satisfy the criterion $\chi^2/\text{d.o.f} \leq 1$, we varied the minimum sink time t_f^{min} and implemented a temporal cutoff t_{cut} , restricting the current insertion to the interval $[t_{\text{cut}}, t_f - t_{\text{cut}}]$. We use smaller t_f^{min} and t_{cut} in the three-state fits than the corresponding two-state fit, within the constraint of $\chi^2/\text{d.o.f} \leq 1$. The extracted charges $g_{S,T}$ are summarized in Table II, with the values of N_{st} used to generate the general-purpose blending data. For the specific case of $g_{S,T}$, we find that $N_{st} = 30$ is sufficient to saturate the statistical uncertainty. The three-state fit results are selected as our primary values, and the systematic uncertainty associated with excited-state contamination is estimated from their difference with the two-state fit results.

The statistical uncertainties of the renormalization constants $Z_{S,T}$ are independent across ensembles and are combined in quadrature with the uncertainties of the bare nucleon matrix elements. In contrast, the systematic uncertainties $\delta_{\text{sys}}Z_{S,T}$ —arising from the truncation of the perturbative matching series, the value of the strong coupling, and scale evolution—are fully correlated. To account for this, we perform the global fit again using the shifted renormalization constant $Z_{S,T} + \delta_{\text{sys}}Z_{S,T}$, and take the difference from the central fit as the systematic uncertainty attributable to renormalization.

For the continuum, chiral and infinite-volume extrapolations, we use the Akaike information criterion (AIC) to estimate the systematic error from different extrapolation models, with the AIC weight we used here are [55]:

$$\omega_i = \frac{\exp\left[-\frac{1}{2}(\chi_i^2 + 2n_{i,\text{par}} - n_{i,\text{data}})\right]}{\sum_j \exp\left[-\frac{1}{2}(\chi_j^2 + 2n_{j,\text{par}} - n_{j,\text{data}})\right]}, \quad (20)$$

where the χ_i^2 , $n_{i,\text{par}}$ and $n_{i,\text{data}}$ refer to the χ^2 , the number of fit parameters and the number of data points for the i -th fit model. The cumulative distribution function(CDF) for the probability distribution of the result is defined as:

$$P(y; \lambda) = \int_{-\infty}^y dx \sum_i \omega_i N_i(x, m_i, \sigma\sqrt{\lambda}), \quad (21)$$

where $N_i(x, m_i, \sigma\sqrt{\lambda})$ is Gaussian distribution with mean m_i and standard deviation $\sigma\sqrt{\lambda}$, and λ is a parameter to control the width of the distribution for extraction systematical error. The median of the CDF is our choice for the central value of y and its total error is given by the 16% and 84% percentiles of the CDF.

$$\sigma_{\text{tot}}^2 = \left[\frac{1}{2}(y_{84} - y_{16})\right]^2 \quad \text{with} \quad P(y_{16}, 1) = 0.16, \quad P(y_{84}, 1) = 0.84. \quad (22)$$

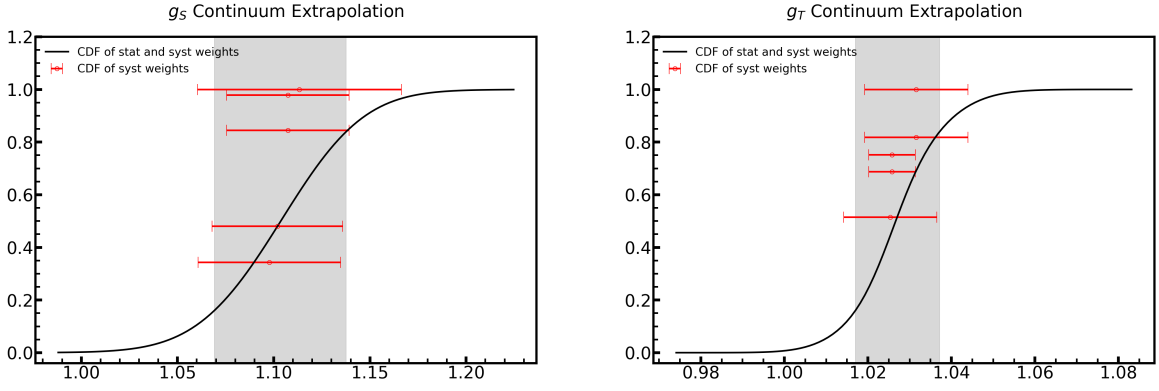


FIG. 11. The CDF of different fit models of the continuum extrapolation of g_S (left panel) and g_T (right panel).

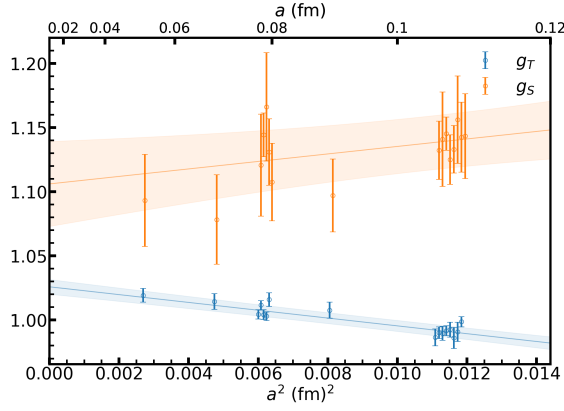


FIG. 12. The lattice spacing dependence of the g_S and g_T with data points corrected to physical pion mass and infinite volume limits. The data points at the same lattice spacing but different pion mass and volume are horizontally shifted to improve readability.

Assuming the systematic error and statistical error are independent, the total error is given by:

$$\sigma_{\text{tot}}^2 = \lambda \sigma_{\text{stat}}^2 + \sigma_{\text{sys}}^2. \quad (23)$$

Then σ_{sys}^2 can be obtained by repeating the analysis with different λ .

1. Continuum extrapolation

For continuum extrapolation, we include the following models in the AIC:

- Simple a^2 form for the $\mathcal{O}(a)$ -improved clover fermion action, $c_a^{(2)} a^2$;
- $a^2 + a^4$ form for higher order correction, $c_a^{(2)} a^2 + c_a^{(4)} a^4$;
- Simple a^2 form with the data at $a < 0.1$ fm only;
- a^2 form with additional $a \log(u_0)$ term for the residual $a\alpha_s$ effect, $c_a^{(1)} a \log(u_0) + c_a^{(2)} a^2$;
- Most conservative $a \log(u_0) + a^2 + a^4$ form, $c_a^{(1)} a \log(u_0) + c_a^{(2)} a^2 + c_a^{(4)} a^4$

As shown in Fig. 11, the extracted $g_{S,T}$ using different fit models are consistent with each other very well.

Figure 12 presents the continuum extrapolation for g_T (blue crosses and band) and g_S (orange dots and band), using the default $a^2 + a^4$ ansatz. The data shown have been corrected for finite-volume effects and unphysical pion

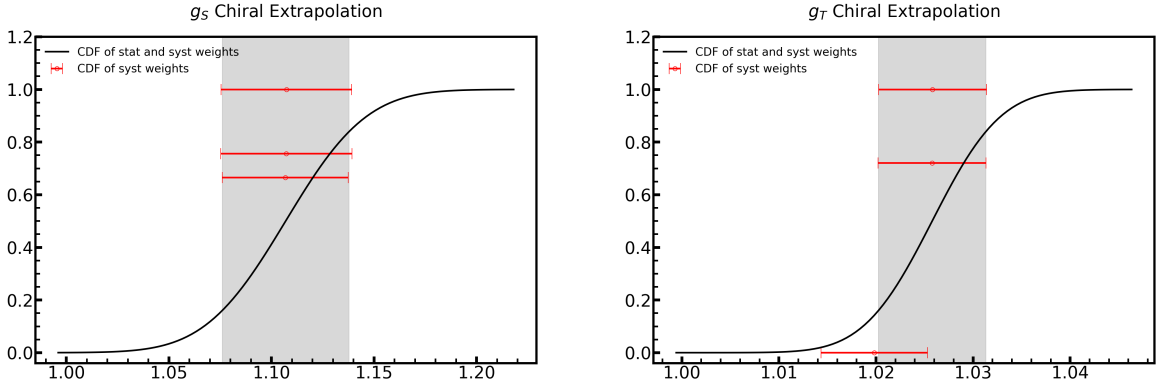


FIG. 13. The CDF of different fit models of the chiral extrapolation of g_S (left panel) and g_T (right panel).

masses using the parameters determined from the global fit. As shown in the figure, results at the five lattice spacings display a clear linear a^2 dependence with no evident a^4 corrections. The slopes for g_S and g_T , however, exhibit opposite signs.

2. Chiral extrapolation

For continuum extrapolation, we include the following 3 models in the AIC:

- Default model with linear light quark mass $m_q \propto m_\pi^2$ dependence and also non-linear correction for heavier pion mass as suggested by χ Pt, $c_l^{(2)} m_\pi^2 + c_l^{(3)} m_\pi^3$;
- Simplified model with the linear term only, $a c_l^{(2)} m_\pi^2$;
- Most conservative one with even higher order term, $c_l^{(2)} m_\pi^2 + c_l^{(3)} m_\pi^3 + c_l^{(4)} m_\pi^4$

As shown in Fig. 13, the extracted $g_{S,T}$ using different fit models are consistent with each other very well, since our $g_{S,T}$ at the physical pion mass have been quite precise. Thus, different fit models are found to produce nearly identical results at the physical pion mass but can exhibit pronounced differences at heavier pion masses.

3. Infinite volume extrapolation

Since the HB χ PT FVE ansatz $m_\pi^2(m_\pi L)^{-1/2} e^{-m_\pi L}$ is disfavored by the g_S data, we consider a general FVE model $m_\pi^i(m_\pi L)^{j/2} e^{-m_\pi L}$ with $i \in \{0, \pm 1, \pm 2\}$ and $j \in \{0, \pm 1, \pm 2\}$ in the AIC average. Those models cover both the HB χ PT FVE ansatz and also naive $e^{-m_\pi L}$ one which is consistent with that of nucleon mass.

Fig. 14 shows a relatively strong dependence of the extracted g_S and g_T on different finite-volume ansatz, highlighting a sizable systematic uncertainty, especially for g_S . The fit quality favors the naive ansatz $e^{-m_\pi L}$ ($\chi^2/\text{d.o.f.} = 0.46$) over the HB χ PT form $m_\pi^2(m_\pi L)^{-1/2} e^{-m_\pi L}$ ($\chi^2/\text{d.o.f.} = 2.5$) for g_S , but the $\chi^2/\text{d.o.f.}$ using either HB χ PT or naive ansatz is smaller than 1 for g_T . The ambiguous result for g_T is expected, as its small finite-volume effects are comparable to the current statistical uncertainties, making the ansatz indistinguishable.

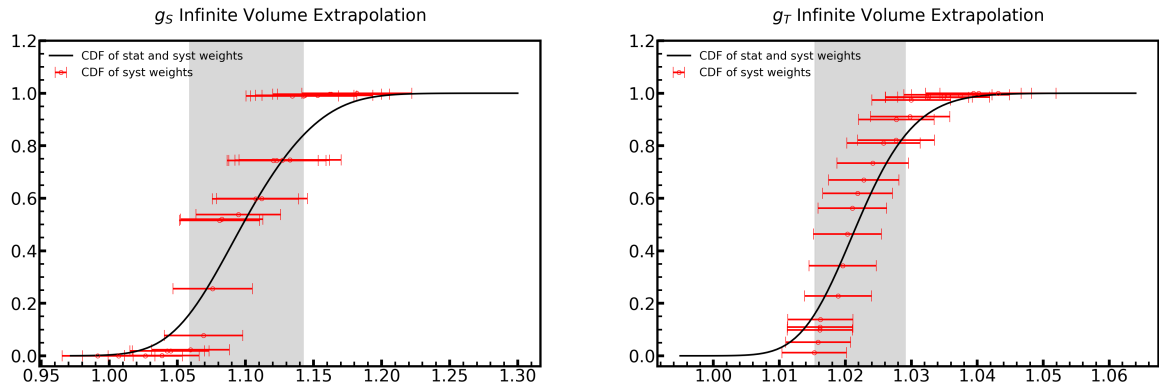


FIG. 14. The CDF of different fit models of the infinite volume extrapolation of g_S (left panel) and g_T (right panel).